

A method for characterizing transient ionospheric disturbances using a large radiotelescope array

A. R. Jacobson¹ and W. C. Erickson²

¹ Atmospheric Sciences Group, Space Science and Technology Division, Mail Stop D466, Los Alamos National Laboratory, Los Alamos, New Mexico 87545, USA

e-mail: 083044@essdp2.LANL.gov (INTERNET); tel: (505)667-9656

² Astronomy Program, University of Maryland, College Park, Maryland 20742, USA

Received June 13, accepted October 11, 1991

Abstract. Radio interferometers have been previously used for study of wave-like disturbances in the overhead ionosphere. However, all such studies involved baselines (≤ 3 km) which were very short compared to the disturbance wavelength, so that meaningful lag information was unavailable, and hence the waves' phase velocity usually could not be measured. Recently we have employed the Very Large Array radiotelescope at 90-cm radio wavelength to study ionospheric waves possessing disturbance wavelengths > 20 km, using baselines which extend to 35 km. We have developed an analysis algorithm which fits spatially monochromatic plane waves ($e^{-ik \cdot r}$ horizontal spatial dependence of the plasma disturbance) for each angular frequency ω in the visibility-phase data. Over the band $\omega/(2\pi) = 0.00025\text{--}0.032$ Hz, this simple plane-wave model accounts for most of the baseline phase structure. The lower frequencies [$\omega/(2\pi) \leq 0.001$ Hz] are observed to be dominated by slow (phase speeds ≤ 0.2 km s⁻¹) acoustic-gravity waves, with a wide range of propagation directions. However, the higher frequencies [$\omega/(2\pi) \geq 0.002$ Hz] are dominated by faster-propagating (≥ 0.2 km s⁻¹) waves tending to be directed toward magnetic east. The latter had never been resolved before this study. The entire spectrum of ionospherically-imposed phase disturbances frequently accounts for > 1 rad of transient baseline visibility phase and thus serves to blur synthesized images. However, the close fit of the phase data to the simple, few-parameter plane-wave model raises the possibility of dynamically compensating transient ionospheric visibility phases prior to forming images, using auxiliary data from a sparse subarray. This paper examines (1) analysis procedures appropriate to long-baseline interferometers, and (2) the basis for dynamic phase compensation using continual wave-parameter fits.

Key words: data analysis – earth: atmosphere – interferometry – scintillation

1. Introduction

Radio-interferometers have been used for studying scintillations since the early days of radio-astronomy (Hewish 1951; Bolton et

al. 1953). They have been used as well for studying travelling ionospheric disturbances (TIDs), starting with the observations of Bougeret (1981) on the Nançay Radioheliograph. That instrument's subsequent, more systematic application to the study of TIDs was reported by Mercier (1986a, 1986b), by Mercier et al. (1989), and by Van Velthoven et al. (1990). Elsewhere, observations have been performed at the Westerbork Synthesis Radio Telescope (Kelder & Spoelstra 1987; Spoelstra & Kelder 1984; Van Velthoven 1990) and at the Clark Lake Radio Observatory (Erickson et al. 1988; Jacobson et al. 1991). The TIDs were mainly ascribable to acoustic-gravity waves (AGWs) in the upper atmosphere.

The common feature of all those observations was that the instrument baselines (≤ 3 km) were much shorter than the TIDs' horizontal radian wavelengths $\lambda/(2\pi)$ (typically ≥ 20 km). As shown by Mercier (1986b), under such circumstances one usually can measure the TID's azimuth *only modulo 180°* as well as only the horizontal *gradient* in the line-of-sight total electron content (TEC). One can *not* measure either the horizontal phase velocity or the amplitude of the TEC perturbation. Very rare exceptions to this limitation come about when the ionospheric refraction is strong enough to cause focussing (on the ground) of radio waves, for which condition Mercier et al. (1989) have shown how to obtain the full wave parameters by using information from simultaneous observations at two radio frequencies.

The observations described in this paper were obtained in 1990 with the Very Large Array (VLA) in New Mexico (Thompson et al. 1980). This array of twenty-seven 26-m telescopes was operated in the 300-MHz range. In this frequency range ionospheric phase deviations greatly dominate those of all other origins. In its most extended configuration the array incorporates baselines up to 35 km in length.

The present article describes a method suitable for *large* radio interferometers, such as the VLA, in which the baselines' dimensions are comparable to the waves' horizontal radian wavelengths $\lambda/(2\pi)$. This regime is frequently occupied by the VLA. We will use our results to test the basis of dynamically compensating ionospheric phase effects on radio-images, for low frequencies ($f < 1$ GHz) where, in some regimes, such effects can limit image quality. A separate publication will describe the ionospheric- and space-physics content of the data.

Send offprint requests to: A. R. Jacobson

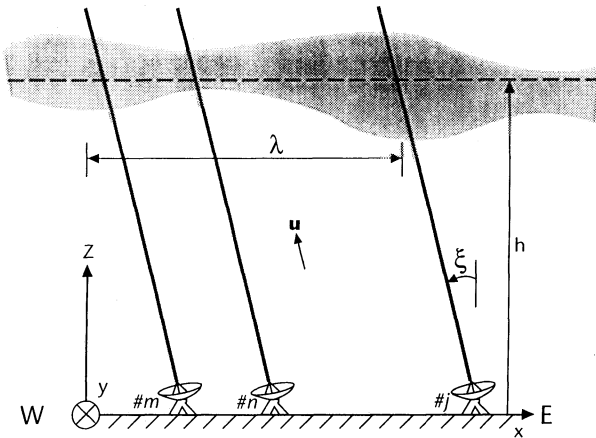


Fig. 1. Schematic of radiotelescopes ranged along the x -axis (eastward) in the vertical/EW plane. The unit vector \mathbf{u} points toward the radiosource. The x -dependent TEC is represented by the shaded undulation at mean height h . The dominant wavelength in the undulation is λ .

2. Basic approach

2.1. Idealized problem

Exceptionally bright, unresolved radiosources can be used to “back-illuminate” the ionosphere so that ionospheric refraction effects can be studied at ground level. Consider the case of two dimensions, say x (horizontal eastward) and z (vertical with respect to ground), as shown in Fig. 1. The unit vector toward the sources is \mathbf{u} , and we have $u_x = -\sin \xi$. Three antennas ($\#m, n, j$) observe a point-source along parallel but displaced paths through an inhomogeneous ionosphere (schematized by the TEC undulation situated at mean height h , with wavelength λ). The TEC, or electron density n_e integrated along the line of sight ds , can be expressed in terms of added electrical phase of the radio wave at, say, antenna $\#m$:

$$\phi_m^{\text{source}} \propto \int_{x=x_m, y=y_m, z=0}^{\text{source}} n_e ds. \quad (1)$$

The superscript “source” on the phase indicates that the TEC depends both on the horizontal intersection point of the ray with the ground (here at $x = x_m$) and on the source position, that is, on the angle through the ionosphere. (Note: Throughout, it will be understood that a function whose argument is omitted, such as ϕ_m above, is of time t , not of angular frequency ω . If we wish to indicate the Fourier transform of the function, then we explicitly include the argument ω .) The dashed level in Fig. 1 is an equivalent phase screen (Hewish 1951) whose x -dependence is taken, say, as

$$\phi(x) = \phi_0 \cos(k(x - x_0)) \quad (2)$$

where $k (= 2\pi/\lambda)$ is the TEC undulation’s wavenumber. For distances (after passing through the phase screen) much exceeding the length L_0 given (Hewish 1951; Salpeter 1967) by

$$L_0 \equiv k_{\text{rf}}/k^2 \quad (3)$$

the radio-frequency field undergoes significant diffraction; for much smaller distances and for a shallow ($\phi_0 \ll 1$ rad) phase screen, diffraction is unimportant, and the rf propagation is ray-

like. However, if $\phi_0 > 1$ rad, the rf rays can be focussed, at a focal distance given (Hewish 1951; Salpeter 1967) by

$$F_0 \equiv L_0/\phi_0. \quad (4)$$

In the case of focussing, Meyer-Vernet et al. (1981) have shown that the focal-plane pattern is not a simple focus but rather a focus plus diffraction sidelobes, at least for point radio sources. In order to ignore diffraction and focussing, then, we require (in terms of Fig. 1) that

$$h/\cos \xi \ll L_0, F_0. \quad (5)$$

It turns out that in the circumstances typical of our observations ($\lambda_{\text{rf}} < 1$ m; screen-antenna slant distance < 600 km; $\lambda > 50$ km; $\phi_0 < 5$ rad) Eq. (5) is robustly satisfied. Thus we may interpret the ionospherically induced electrical phase perturbations at each antenna as a straightforward sampling of the phase screen *locally* where the *undisturbed* ray passes through the screen. We do not treat diffraction or scintillation phenomena in this work.

To describe the ray in three dimensions, we introduce the horizontal northward direction y and an additional angle η ; the ray unit vector is then

$$\begin{aligned} \mathbf{u} &= (u_x, u_y, u_z) \\ &= (-\sin \xi, \sin \eta, \sqrt{1 - \sin^2 \xi - \sin^2 \eta}). \end{aligned} \quad (6)$$

The no-diffraction, no-focussing condition becomes

$$h/\cos Z \ll L_0, F_0 \quad (7)$$

where Z is the zenith distance. The azimuth A (reckoned clockwise from N) and Z are related to ξ and η by

$$\sin \xi = -\sin Z \sin A \quad (8a)$$

and

$$\sin \eta = \sin Z \cos A \quad (8b)$$

2.2. Model of plane-wave TEC perturbation

We will model the phase-screen disturbance sensed by an antenna at $\mathbf{r} = (x, y, 0)$, at a given angular frequency ω , as the real part of a spatially monochromatic plane wave whose temporal Fourier coefficient is

$$\hat{\phi}(\omega) = A(\omega) \exp\{-i\mathbf{k} \cdot \mathbf{r}\} \quad (9)$$

where $A(\omega)$ is the complex amplitude and \mathbf{k} is implicitly a function of ω . (The circumflex is used only for modeled quantities.) Then the modeled Fourier coefficient of the relative electrical phase of the signal at antenna $\#n$, with respect to that at $\#m$, is

$$\begin{aligned} \hat{\phi}_{mn}(\omega) &= A(\omega) [\exp(-i\mathbf{k} \cdot \mathbf{r}_n) - \exp(-i\mathbf{k} \cdot \mathbf{r}_m)] \\ &= -2i A(\omega) \sin(\mathbf{k} \cdot \mathbf{d}_{mn}) \exp(-i\mathbf{k} \cdot \mathbf{c}_{mn}) \end{aligned} \quad (10)$$

where the baseline “centroid” vector is

$$\mathbf{c}_{mn} \equiv \frac{\mathbf{r}_n + \mathbf{r}_m}{2} \quad (11a)$$

and the baseline “difference” vector is

$$\mathbf{d}_{mn} \equiv \frac{\mathbf{r}_n - \mathbf{r}_m}{2} \quad (11b)$$

which is half the usual baseline vector

$$\mathbf{b} \equiv \mathbf{r}_n - \mathbf{r}_m \quad (11c)$$

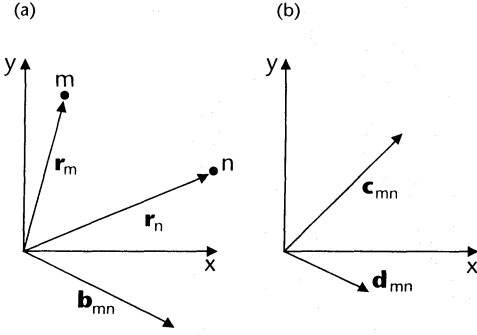


Fig. 2a and b. Plan views in the horizontal plane of vectors associated with the baseline containing antennas # m and # n , with reference to Eq. (11): **a** Antenna position and baseline vectors; **b** centroid and difference vectors

Figure 2 illustrates the relationship of the position, baseline, centroid, and difference vectors. It is simple to show that Eq. (10) is consistent with the more general result, Eq. (2) of Meyer-Vernet (1980), in the limit where the observer is very close to the phase screen.

Equation (10) shows that the visibility phase's Fourier coefficient on baseline m, n will have a phasing (related to the temporal signal's lag) controlled by the position of the baseline's *centroid* vector, via the complex exponential, and a signed sensitivity controlled by the *difference* vector, via the sine function. The factor of 2 in Eq. (10) arises because the baseline Fourier coefficient is based on a *difference* of phase between two stations.

The short-baseline limit of Eq. (10) is

$$\lim_{\substack{|d_{mn}| \rightarrow 0 \\ |c_{mn}| \rightarrow 0}} \hat{\phi}_{mn}(\omega) = -2i A(\omega) \mathbf{k} \cdot \mathbf{d}_{mn} = \mathbf{b}_{mn} \cdot \lim_{\substack{|d_{mn}| \rightarrow 0 \\ |c_{mn}| \rightarrow 0}} \nabla \hat{\phi}(\omega). \quad (12)$$

This agrees with the formula of Mercier (1986b), the only difference being that we deal with $\nabla \phi$, which has units of electrical phase per unit distance, whereas Mercier deals with a quantity $\mathbf{G} (\equiv \nabla \text{TEC})$, which has units TEC per unit distance. In this short-baseline limit, the complex exponential has been ordered away, and the information on lag, and hence phase speed, is lost. The azimuth, modulo 180° , can be inferred (Mercier 1986b) from the direction of the instantaneous gradient in Eq. (12).

2.3. Relevance to dynamic compensation of ionospheric phase

An image formed from baseline visibilities (correlations), whose phases are affected by ionospheric waves by the model of Eq. (10), will undergo translation and blurring. The translation will arise when $\omega^{-1} > (\text{image integration time})$ and $k^{-1} > (\text{longest baselines})$. The blurring will occur for $k^{-1} \ll (\text{longest baselines})$ and any ω^{-1} , or for $\omega^{-1} < (\text{image integration time})$ and any k^{-1} . One of the motivations of this work is to determine the feasibility of dynamically compensating these effects, by integrating visibilities for durations $\leq \omega^{-1}$ and by *fitting and removing the wave contributions to the visibilities' phases prior to image formation*. The present study is confined to bright, unresolved sources, knowledge of which, *by itself*, would not justify such compensation. Rather, the ultimate application, to improve images of diffuse or weak radio fields, would require exploiting the nearby brighter radio-objects as ionospheric calibrators. *The basic prerequisite for this concept to be worth pursuing, whatever the ultimate technical approach, is to show that Eq. (10), or an elaboration thereof, can*

model the bulk of ionospheric transient phase structure. The present work aims to determine whether this prerequisite is indeed satisfied.

3. Non-ideal effects

3.1. Source confusion

Ideally one would fit the baseline-phase raw data's Fourier coefficients to the model of Eq. (10) and immediately derive the wave parameters $A(\omega)$ and \mathbf{k} . Unfortunately, at low frequencies (e.g., 307.5 and 333.0 MHz as used in our observations), the individual telescope beams are as wide as 2.5° and are thus likely to contain secondary sources in addition to the primary source. Even if the primary ("p") is much stronger than the secondary ("s") source, the confusion phase effects can be considerable, in view of our interest in *resolving baseline phases to a small fraction of a radian*. The diurnal rotation of the celestial sphere causes the m, n baseline phase (here labeled ψ , for the case of phase progression caused purely by geometry) due to the p (or s) electric fields to vary, vs. local sidereal time T , as

$$\frac{\partial \psi_{mn}^{p(s)}}{\partial T} = k_{\text{rf}} \mathbf{b}_{mn} \cdot \left(\frac{\partial \sin \xi_{p(s)}}{\partial T}, \frac{\partial \sin \eta_{p(s)}}{\partial T} \right). \quad (13)$$

While image formation would separate these sources in the image space, the task of deriving the ionospheric wave parameters is much simpler in the visibility space. Thus we shall continue to work with visibilities, but in an altered form that in effect invokes phase closure to favor the primary source.

Suppose the raw visibilities are fringe-compensated ("stopped") for the p source. Then the *residual* fringe progression on the s source's contribution to the visibility is what concerns us, because its interference with the p source's contribution will cause a spurious net phase oscillation in the total visibility. Let us assume for simplicity that each source is equally visible, i.e. that it is in the primary telescope field of view and is not vignetted by receiver-bandwidth effects. Let us define a characteristic angular frequency

$$\begin{aligned} \Omega_{mn} &\equiv \frac{\partial \psi_{mn}^s}{\partial T} - \frac{\partial \psi_{mn}^p}{\partial T} \\ &= k_{\text{rf}} \mathbf{b}_{mn} \cdot \left(\frac{\partial \Delta \sin \xi}{\partial T}, \frac{\partial \Delta \sin \eta}{\partial T} \right) \end{aligned} \quad (14)$$

where " Δ " signifies the value for the s , relative to the p , sources. (Formulae for the derivatives in the vector above are given in Appendix A.) Defining the p (or s) electric field as $E_{p(s)}$, the total visibility can then be shown to vary in terms of Ω as

$$V_{mn} \propto |E_p|^2 + |E_s|^2 \exp(i \Omega_{mn} T). \quad (15)$$

The visibility's spuriously oscillating phase (indicated by ε) is

$$\varepsilon_{mn} = \tan^{-1} \left\{ \frac{|E_s|^2 \sin(\Omega_{mn} T)}{|E_p|^2 + |E_s|^2 \cos(\Omega_{mn} T)} \right\}. \quad (16)$$

In the limit

$$\frac{|E_s|^2}{|E_p|^2} \ll 1$$

the total visibility's spurious phase simplifies to

$$\varepsilon_{mn} \cong \frac{|E_s|^2}{|E_p|^2} \sin(\Omega_{mn} T). \quad (17)$$

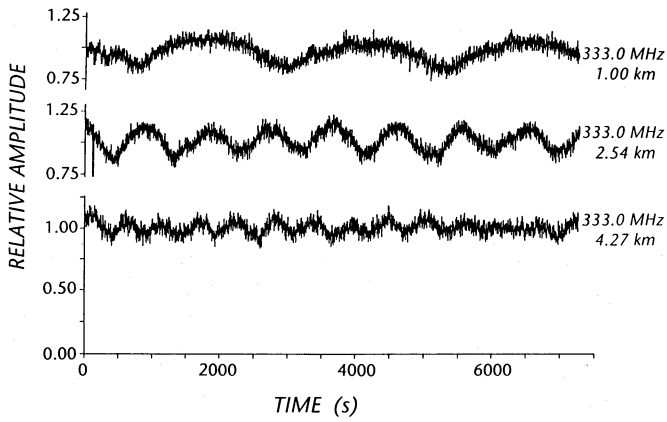


Fig. 3. Relative visibility amplitude vs. time (note breaks in ordinate scale) for three short, parallel baselines, all at one radio frequency, for right-hand-circular polarization. The amplitude modulation is due to source confusion. These VLA “A-configuration” observations and those of Figs. 5–10 were of source 1419+064 during 2 h starting at 08:33:02 UT on 9 March 1990. The source position in the local sky (see Eq. 8) evolved from $(\sin \xi, \sin \eta) = (-0.457, -0.401)$ to $(\sin \xi, \sin \eta) = (+0.051, -0.463)$ during those 2 h

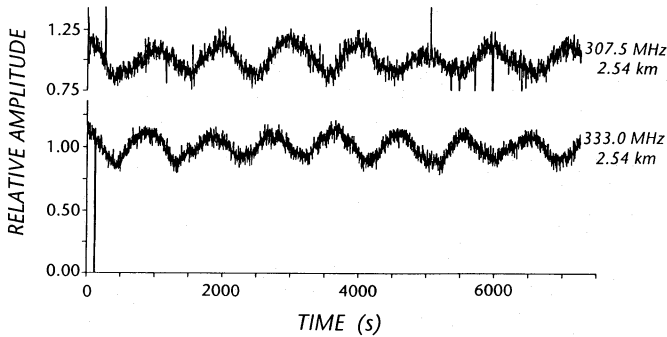


Fig. 4. Relative visibility amplitude vs. time, for two radio frequencies on a single short baseline, for right-hand-circular polarization. The spikes are due to terrestrial radio interference

From Eqs. (14–17) we infer that these spurious oscillations have the following properties:

(1) Both amplitude and phase of the m, n visibility will oscillate with angular frequency Ω_{mn} , although in quadrature with each other.

(2) Ω_{mn} will vary as the baseline’s scalar product with the time-rate-of-change of the p-to-s separation vector in the space $(\sin \xi, \sin \eta)$. Thus, for two parallel baselines, the frequency will vary as the length. For one baseline, the frequency will also vary as the time-rate-of-change of the p-to-s separation vector.

(3) Ω_{mn} will vary as k_{rf} and hence as the radio frequency f .

We exemplify this behavior with actual VLA data. Figure 3 shows relative amplitude vs. time of the visibilities on three parallel and rather short baselines. The dominant oscillation frequency scales as the baseline length, consistent with property (2) above. (The oscillation amplitude on the longest baseline is starting to be suppressed because of the s source’s reduced visibility due to receiver bandwidth, which occurs first on the longest baseline.) Figure 4 compares the relative amplitudes at two receiver frequencies, both on the same baseline. Note that the additional $\approx 1/2$ cycle of the phase oscillation executed at 333.0 MHz, relative to 307.5 MHz, is consistent with property (3) above.

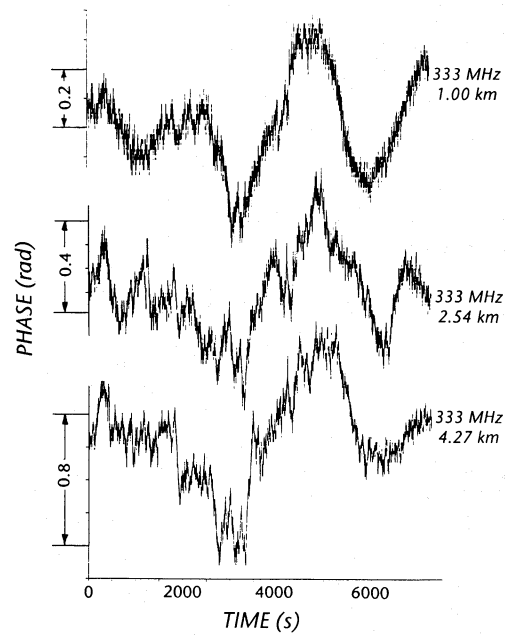


Fig. 5. Phase vs. time of raw visibility (for the same three short, parallel baselines used in Fig. 3) at 333.0 MHz, right-hand-circular polarization. The dissimilarities between the three traces’ shapes, and the amplitudes’ imperfect scaling with baseline length, are a phase manifestation of source confusion

The spurious oscillations have an effect on the visibility phase, as shown in Fig. 5. The data are from the same visibilities as are the data of Fig. 3. The ordinate scales are provided to show that the disturbance amplitudes *do not* scale with baseline length. In particular, note the shortest (1-km) baseline’s phase shows a sinusoidal oscillation which is synchronized with that baseline’s amplitude oscillation (see Fig. 3, top trace). We submit that this discrepancy in the short-baseline phases is due to source confusion. The next section shows one way of mitigating such effects of confusion.

3.2. Software mitigation of source confusion

At the VLA the signals are cross-correlated between every baseline pair of the $N=27$ array elements in $N(N-1)/2 = 351$ complex correlators. These data are required to map an extended source region. However, in our case, the primary source that we observe is unresolved and produces a plane wave above the ionosphere, so that we need to determine only the ionospherically induced phase shifts in the ray paths from the source to each element of the array. One element must be used as a phase reference, so the totality of the ionospheric information is contained in the phases of the other $N-1$ elements relative to this reference element. In the absence of any secondary sources the phases on all of the $N(N-1)/2$ baselines could be predicted exactly from the $N-1$ element phases, and the extra baseline phases would contain no new information. However, these $N(N-1)/2$ baseline phases do contain information about *secondary* sources, and a variation of phase closure can be used to mitigate the spurious effects that secondary sources produce. In a manner similar to that of Cornwell & Wilkinson (1981), we average the data over the baselines in order to favor the p source’s contribution and to disfavor the s source’s contributions. Let $\#m$ be the reference element and consider the average (denoted by “ $\langle \dots \rangle$ ”)

$$\langle \Phi \rangle_{mn} \equiv \frac{1}{N-1} \left(\Phi_{mn} + \sum_{j=1, j \neq m, n}^N [\Phi_{jn} - \Phi_{jm}] \right) \quad (18)$$

where Φ_{mn} is the total (ionospheric plus spurious) *measured* phase. (Note that the *total* measured phase is indicated by an *upper-case* Φ . Lower-case ϕ indicates *ionospheric* phase.) The ionospherically generated phase (see Eq. 1) for, say, the p source, is a conservative function of antenna position $\mathbf{r} = (x, y, 0)$, so the ionospheric contributions to the baseline phases, due to the p source, must obey phase closure:

$$\phi_{jn}^p - \phi_{jm}^p = \phi_{mn}^p \quad (19)$$

etc. Thus if the p source were the only source and were absolutely unresolved, Eq.(18) would reduce to the trivial form $\langle \Phi_{mn} \rangle = \Phi_{mn}$. To treat the realistic case of *ionospheric plus confusion effects*, though, we rework the development of Eq. (17) as follows: The complex visibility on baseline m, n will be (to within a constant amplitude factor)

$$V_{mn} \propto |E_p|^2 \exp(\phi_{mn}^p) + |E_s|^2 \exp(i\Omega_{mn}T + \phi_{mn}^s). \quad (20)$$

This is analogous to Eq. (15) but with ionospheric phase shifts included. The measured phase (including both ionospheric and confusion effects) is thus

$$\Phi_{mn} = \phi_{mn}^p + \tan^{-1} \left\{ \frac{|E_s|^2 \sin(\Omega_{mn}T + \phi_{mn}^s - \phi_{mn}^p)}{|E_p|^2 + |E_s|^2 \cos(\Omega_{mn}T + \phi_{mn}^s - \phi_{mn}^p)} \right\} \quad (21)$$

in analogy to Eq. (16). Again assuming that the secondary source is much weaker than the primary, this simplifies to

$$\Phi_{mn}^p \cong \phi_{mn}^p + \frac{|E_s|^2}{|E_p|^2} \sin(\Omega_{mn}T + \phi_{mn}^s - \phi_{mn}^p) \quad (22)$$

in analogy to Eq. (17). Substituting Eq. (22) into Eq. (18) and invoking phase closure (Eq. 19), we get finally

$$\langle \Phi \rangle_{mn} \cong \phi_{mn}^p + \frac{1}{N-1} \frac{|E_s|^2}{|E_p|^2} \left\{ \begin{aligned} &\sin(\Omega_{mn}T + \phi_{mn}^s - \phi_{mn}^p) \\ &+ \sum_{j=1, j \neq m, n}^N [\sin(\Omega_{jn}T + \phi_{jn}^s - \phi_{jn}^p) - \sin(\Omega_{jm}T + \phi_{jm}^s - \phi_{jm}^p)] \end{aligned} \right\}. \quad (23)$$

The first term on the rhs is the ideal single-source phase due to the ionosphere. The confusion effect in braces is scaled by the ratio of s to p electric intensity and contains $N-1$ terms whose frequencies Ω are *different for different baselines*. Provided we *avoid* primarily using translated but otherwise identical baselines, these terms develop differently (vs. time), so that at any moment they are mutually random. Thus the root mean square (rms) of their sum (in braces) is only $\approx (N-1)^{1/2}$ times the rms of individual terms, so that the *relative* scaling with N of the averaged confusion effect, relative to the ideal term, is $\approx (N-1)^{-1/2}$. We see that $\langle \Phi_{mn} \rangle$ becomes an increasingly accurate estimator of the ideal effect ϕ_{mn}^p as $N-1$ increases. Moreover, the baseline-averaged phase data require only $\approx 2/N$ the space that the raw phases do.

Figure 6 shows the baseline-averaged phases on the same three baselines whose raw phases were shown in Fig. 5. Note that the three traces in Fig. 6 are more congruent and that they scale more closely as the baseline length (as is roughly expected, since even the 4.27-km baseline will be shown not to exceed k^{-1} through most of the spectrum of the disturbance), compared to the traces in Fig. 5. We implement the baseline-averaging on all data as a matter of

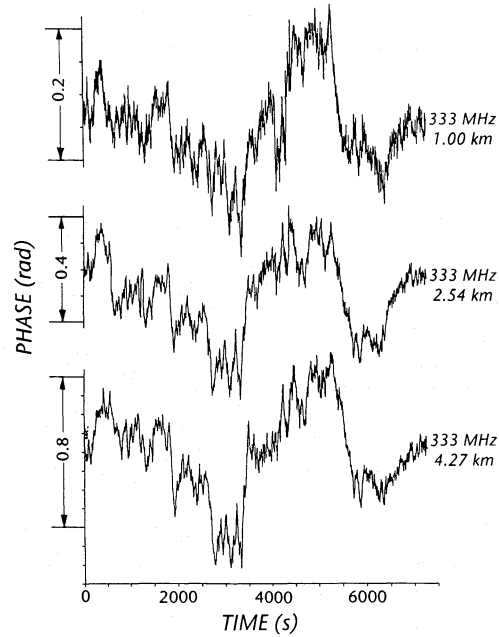


Fig. 6. “Baseline-averaged” phase vs. time for the same three baselines as in Fig. 5, for 333.0 MHz, right-hand-circular polarization. The waveforms are now more similar in shape and scale more closely with baseline length than do those in Fig. 5

course. It is done in the time domain, before Fourier transformation, so that only $N-1$ Fourier transforms are required.

Finally, we note that the effects of source confusion are further mitigated by the intended fit to a plane-wave model given by Eqs.(9 and 10). Provided that our baselines are not primarily equal-length, parallel, and only displaced from each other (and it is hard to imagine why such an incomplete array would be chosen), the confusion phases are period-dispersed between baselines. This militates against their affecting the wave model, in which the Fourier coefficients of various baselines phases *at any given frequency* have a definite coherent relationship.

3.3. Excision of samples affected by terrestrial interference

The raw amplitude data in Fig. 4 exhibit several samples that are obviously heavily contaminated by rf interference. Our standard data-reduction process removes such samples from the raw time-series data, prior to path averaging. Excision is triggered whenever the magnitude of the sample-to-sample complex visibility *change* exceeds a critical fraction ($=0.25$) of the mean magnitude. Excised points are interpolated. Because of the short sampling interval ($=1.67$ s) compared to any $2\pi\omega^{-1}$ (≥ 30 s) we have observed, the effect of excising interference-contaminated data is only beneficial. Had we sampled and stored the visibilities less frequently, say only at the Nyquist period (15 s), the excisions would have been more likely to corrupt the Fourier coefficients near the observed 30-s-period limit.

3.4. Removal of secular trends

The individual data sets have durations 1500–7200 s. There are frequently noticeable offsets and slow trends in the baseline phases associated with longer timescales. Following Mercier (1986b), we fit a pedestal and a slope to each time series in the baseline-averaged data and subtract these two effects prior to windowing

and Fourier transformation. This step removes very slow ionospheric effects such as diurnal electron-density variations.

4. Ionospheric-wave observational study

4.1. The database

The data were gathered on the VLA (Thompson et al. 1980) intermittently between 9 March and 11 September 1990. The VLA is located at $107^{\circ}6'W$ and $34^{\circ}N$. Most of the data were gathered in “A-configuration”, whose maximum baselines extend nearly 36 km. During July–September the VLA was in “B-configuration”, with baselines scaled down by a factor of three. There were 49 observing sessions totaling ≈ 36 h, with individual sessions lasting between 1500 and 7200 s. These sessions were selected to exploit breaks in the VLA’s astronomical observing program. Data were gathered simultaneously at two center frequencies (307.5 and 333.0 MHz) and on both circular polarizations, for a total of 4 channels. The receiver bandwidth was 3 MHz for the upper frequency and 6 MHz for the lower. Visibilities were recorded at the fastest available rate (once each 1.67 s). A strong unresolved radiosource was chosen, usually closest to transit during each observing session. Of the 49 sessions, one lacked half the channels, and another employed such a low-elevation (18°) source as to be unuseable (in terms of this study) due to significant amplitude modulation, possibly of the same ionospheric origin as studied by Mercier et al. (1989). There remained 47 sessions in which the instrument functioned adequately and during which the ionospheric effects were in the “weak scattering” regime (see Eq. 7). The line-of-sight to the source typically lies closer to the zenith than $Z = 45^{\circ}$, although in a couple of cases the limit is $Z = 65^{\circ}$. The significance of this in the present work is only that our data have lines-of-sight that are typical of those used in the VLA’s usual astronomy applications. Elsewhere, we will investigate the ionospheric wave activity’s different effects on various lines of sight.

The baseline-averaged phase data were first checked to verify that the phase excursions scaled (between the two center frequencies) as $1/f$, in order to be confident that they originate in free-electron refractivity. The expected scaling is approximately confirmed, both in individual sessions and averaged over the entire database: In the band 0.00025–0.02 Hz, the database-averaged ratio of phase variance summed over all baselines (for $f = 307.5$ MHz : $f = 333.0$ MHz) is 1.15, while the ideal ratio would be 1.17.

4.2. Example of a single observing session

For the same session whose short-baseline data are discussed in connection with Figs. 4–7, we show three long-baseline phase time series (derived from baseline-averaged data) in Fig. 7. The three baselines are each ≈ 21 km long and extend along the three VLA arms, which point approximately west-southwest (“SW”), east-southeast (“SE”), and north (“N”). All three baselines show phase periodicities from < 200 s to > 4000 s. However, the N arm’s short-period activity is noticeably weaker than that on the SW and SE arms. This is consistent (Mercier 1986b) with the shorter-period waves’ having azimuths closer to E (or W) than to N (or S). Similarly, the long-period oscillation which dominates on the N arm is weaker on the other arms; this is consistent with that wave’s having an azimuth closer to N (or S) than to E (or W). Both of these rough conclusions will be confirmed by the systematic analysis to follow.

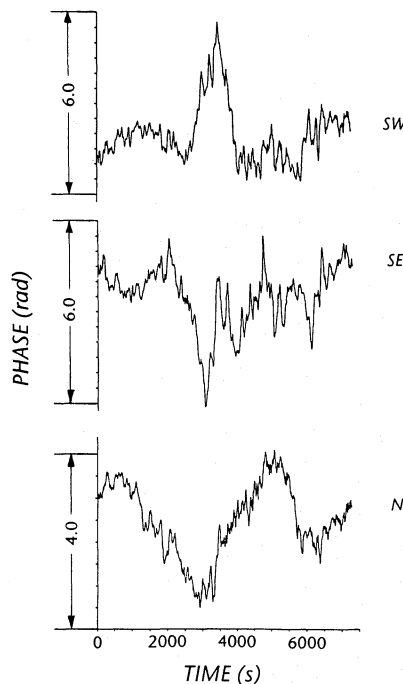


Fig. 7. “Baseline-averaged” phase vs. time for the longest baseline on each of the VLA arms, at 333.0 MHz, right-hand-circular polarization

The baseline-averaged data for all $N - 1$ ($= 26$) non-redundant baselines are then subjected to the plane-wave model of Eq. (10). For $\omega/(2\pi) < 0.001$ Hz, this is done independently for each frequency. Each of the $N - 1$ baselines provides two data (the real and imaginary parts of the measured Fourier coefficient $\Phi_{mn}(\omega)$); the model has four parameters (the two components of \mathbf{k} , and the real and the imaginary parts of $A(\omega)$). Thus the least-squares fit has $2(N - 1) - 4$ ($= 48$) degrees of freedom. For $\omega/(2\pi) \geq 1 \cdot 10^{-3}$ Hz, we fit the amplitude $A(\omega)$ independently for each frequency, but we constrain the slowness $S \equiv k/\omega$ to be constant within each of the five octaves 0.001–0.002 Hz, ..., 0.016–0.032 Hz. This is done to strengthen the statistical significance of the fitted wavenumbers, and was undertaken only after noticing that, apart from statistical variations, the slowness within an octave was sensibly constant. In the constrained- S case, letting M be the number of Fourier frequencies in the octave, the number of data is $2M(N - 1)$, while the number of parameters is $2M + 2$, so that the least-squares fit has $2M(N - 2) - 2$ degrees of freedom.

Figure 8 shows the azimuth (toward which the wave propagates) on the top, and the phase-speed $V \equiv \omega/|k|$ on the bottom, using 333.0 MHz. The solid circles indicate results from fitting the right-hand circular polarization data; the \times symbols are for left-hand circular.

Another realization of random errors in the fitted parameters can be obtained by comparing the results of Fig. 8 with their counterparts using the other radiofrequency channel (307.5 MHz). When we do so (not shown), the same behavior is seen: The azimuth shows less susceptibility than does the phase speed to random errors.

Turning to the content of Fig. 8, we first remark that the lower frequencies (< 0.001 Hz) appear to be dominated by AGWs propagating toward the southwest quadrant with very low phase speeds ($V \leq 0.1$ km s $^{-1}$). However, the higher frequencies are dominated by waves propagating roughly toward magnetic east

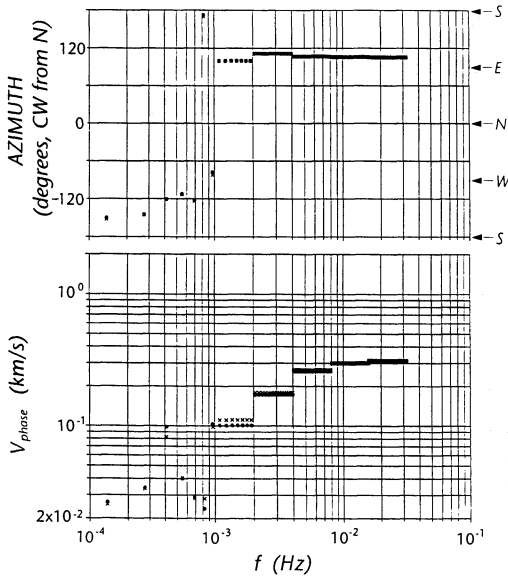


Fig. 8. Least-squares solutions for azimuth and phase speed, vs. Fourier frequency, fitted to the 26 “baseline-averaged” phase records at 333.0 MHz from which Fig. 7’s 3 records were abstracted. Solid and “x” symbols are independent fits from right- and left-hand-circular-polarization data, respectively

(or, at any rate, into the azimuth sector $90^\circ\text{--}115^\circ$) at higher speeds ($0.1 \leq V \leq 0.3 \text{ km s}^{-1}$). One is entitled to ask whether the transition in phase speed at intermediate frequencies is truly a dispersion effect of the higher-frequency waves, or rather, just a compromise solution by the one-wave model (Eq. 10) in the presence of an *overlap* of AGWs and the higher-frequency wave. This suspicion will be discussed further below.

The data presented in Fig. 8 are essentially k vs. ω , presented in terms of the more familiar quantity phase velocity. However, as discussed at length by Marcier (1986b), the line-of-sight to the radiosource is not fixed in the ionosphere, but rather, describes a diurnal revolution. The line-of-sight’s velocity U_{los} through the ionosphere varies according to where the ionospheric wave is located along the line-of-sight, so that some a priori knowledge (or guessing) is needed to make precise the estimate of Doppler shift. However, the measured k is correct from the start, being unaffected by line-of-sight motion, while the apparent angular frequency differs from the “true” angular frequency in the geostationary ionospheric frame by $\Delta\omega = k \cdot U_{\text{los}}$. Typically this Doppler shift causes frequencies to be corrected by $< 20\%$. While the effect of this Doppler shift will be explicitly considered in the paper to follow, following the approach developed by Mercier (1986b), the phenomenon is dealt with here merely by noting that both the ordinate and the abscissa in Fig. 8 are subject to Doppler shifts which must be corrected prior to their interpretation in terms of a wave dispersion relation in the ionospheric medium. At present, though, we are concerned more with the *formal* suitability of a single-plane-wave model (as revealed in its ability to fit the experimental data) than with the physical interpretation of the model parameters. For a *formal* solution of the least-squares model, the Doppler shifts are irrelevant.

In order to help us to assess whether the one-wave model is useful for the data leading to Fig. 8, we show in Fig. 9 the baseline-averaged phase spectrum of the data (solid circles) and of the least-squares residuals (x symbols), both as functions of frequency. Each point is averaged over the two polarizations’ completely independent least-squares fits. If the single-wave model were

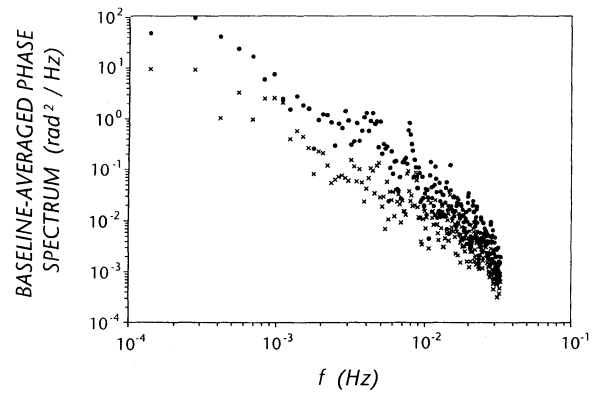


Fig. 9. Phase spectrum averaged over baselines, vs. Fourier frequency, averaged over both polarizations, for the data leading to Fig. 8. Solid and “x” symbols are for the data and for the least-squares residuals, respectively

perfectly able to describe the data, the residuals would be zero. Figure 9 shows that the model is not perfect but nonetheless reduces the residuals-squared severalfold from the level of the data-squared. Note, however, that in the region around $1 \cdot 10^{-3} \text{ Hz}$, the fit is poorer compared to neighboring spectral regions, as revealed by the fact that the residual spectral density is still $\approx 1/2$ of the data spectral density. This may indicate the presence of two overlapping waves, a condition which is likely to occur at this place, since it lies at the approximate boundary between (1) the slow, low-frequency and (2) the faster, high-frequency portions of the spectrum. In the presence of two overlapping waves, the single model will yield compromise parameters and will be less successful in reducing the least-squares residuals, to an extent which depends (1) on the two sets of wave parameters and (2) on the interferometer configuration.

4.3. Database-averaged results

In order to extend the statistical significance of the test of the single-wave model, we have accumulated results analogous to those of Fig. 9 over the *entire database*. The data from the two polarizations were averaged for each session and each radio-frequency, and the latter were then converted to units of ΔTEC (\equiv difference in TEC between the two ends of a given baseline) to make the results independent of rf frequency. Figure 10 shows the baseline-averaged ΔTEC spectrum averaged over the database’s sessions and averaged over octave bands, from 0.00025–0.0005 Hz through 0.016 to 0.032 Hz. The weighting of each session reflects that session’s duration. The solid curve is the spectrum of the data, while the dashed curve is the spectrum of the residuals. Because a data presentation such as Fig. 10 depends on the baseline dimensions, its primary purpose is to determine the efficacy of the single-wave model as a function of wave frequency, rather than to present the plane-wave intensity, which would be independent of baseline length. *Throughout most of the spectrum, the residuals-squared are roughly an order-of-magnitude less than the data.* Thus, we may conclude that most of the TEC-generated visibility-phase perturbations can be fitted to a simple model employing just a single plane wave per Fourier frequency.

Despite this apparent success, an important problem is the inability of the single-wave model to account *completely* for the phase excursions. The resultant *systematic* least-squares errors, in practice, are found to dwarf the random errors. This can be appreciated by considering the phase structure function $\langle(\Delta\Phi)^2\rangle$,

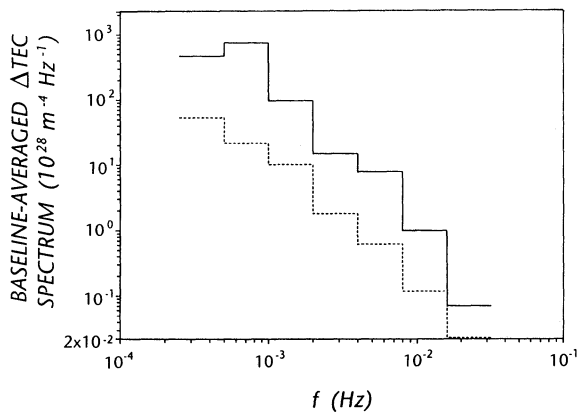


Fig. 10. Differential-TEC (i.e., differenced between the baseline elements) spectrum averaged over baselines, vs. Fourier frequency, accumulated over both polarizations and both frequencies, through the entire database. Solid and dashed curves are for the data and for the least-squares residuals, respectively. Results are binned into octaves

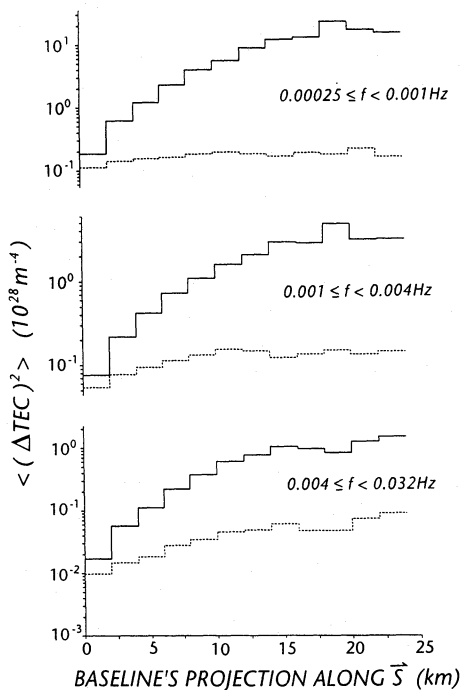


Fig. 11. Differential-TEC spectrum vs. projection of baseline length onto propagation direction, accumulated over both polarizations and both frequencies, through the entire database. The three panels cover different Fourier-frequency passbands. Solid and dashed curves are for the data and for the least-squares residuals, respectively

expressed as a TEC structure function $\langle(\Delta\text{TEC})^2\rangle$ so that both radiofrequencies' data can be averaged together. The structure function depends on the two baseline components, b_x and b_y . However, for each Fourier frequency during each observing session, the direction of the fitted \mathbf{k} is a free parameter and thus varies widely. Our purpose being to test the efficacy of the single-wave model, then, it is instructive to reexpress the structure function in horizontal coordinates x' and y' , which are rotated relative to x and y about the z -axis, and which are respectively parallel and perpendicular to the fitted \mathbf{k} . Furthermore, we note that the plane-wave model can reduce the residual phase structure

along \mathbf{k} but can do nothing about residual phase structure perpendicular to \mathbf{k} . Thus at a given frequency and in a given observing session, we average the phase-structure function (scaled to $\langle(\Delta\text{TEC})^2\rangle$) over b_y' and display the results versus $|b_x'|$, the magnitude of the baseline's projection onto \mathbf{k} or \mathbf{S} . This is shown in Fig. 11 for the data (solid curve) and the residuals (dashed curve) in 2-km bins of $|b_x'|$. Further, the display is done separately for each of three frequency passbands: At the top are the low frequencies, dominated by AGWs; at the bottom are the highest frequencies, which are frequently (but not always) dominated by the faster waves propagating roughly toward magnetic east, and in the center are the transition frequencies.

Figure 11's top panel shows that in the AGW band, the residual $\langle(\Delta\text{TEC})^2\rangle$ is almost constant, rising only slightly versus $|b_x'|$. Also, at large $|b_x'|$ the residual $\langle(\Delta\text{TEC})^2\rangle$ is 10^{-2} of the data $\langle(\Delta\text{TEC})^2\rangle$. This does not contradict the ratio 10^{-1} from Fig. 10, though, because the previous figure involved effectively an average over both b_x' and b_y' , whereas Fig. 11 displays the dependence on b_x' and averages only over b_y' .

In contrast, Figure 11's bottom panel shows that at high frequencies, the residual $\langle(\Delta\text{TEC})^2\rangle$ rises versus $|b_x'|$ albeit less rapidly than does the data $\langle(\Delta\text{TEC})^2\rangle$. The center panel shows that at the transition frequencies, the residuals' behavior vs. $|b_x'|$ is intermediate between that of the low and of the high frequencies.

5. Conclusions and prospects

The VLA baseline-phase time-series data evidently tend to conform to the single plane-wave parametric model (Eqs. 9 and 10). The utility of a parametric model is that, unlike a straightforward spatial Fourier \mathbf{k} -spectrum estimation, the model parameter \mathbf{k} can be resolved much finer than the Nyquist increment implied by the array dimensions. The test of the model's validity, or at least of its efficacy, lies in the ability of the posited single wave to account for most of the phase activity at any given ω . *The model evidently passes this test reasonably well most of the time.* We expect that future elaboration of the model to accommodate, say, *two* simultaneous, waves will improve its ability to describe the data, while at the same time conserving a large number of degrees of freedom. These encouraging results are obtained with baseline dimensions that exceed by only one order of magnitude those of other interferometers for which ionospheric results have been reported. Thus, it is at least possible that for waves of sufficiently low phase speed and sufficiently short period, the other instruments' data may be able to yield phase velocity, not just azimuth modulo 180° , when treated with an analysis algorithm like the one developed here for the VLA.

In principle, the simplicity of the plane-wave model augurs well for the scheme of fitting the wave parameters with data from a sparse subarray and then using the results to remove the wave effects from the main array's visibilities prior to image formation. In other words, because the ionospheric effects can be roughly described by just four parameters per ω , these can be ascertained with a handful of antennas using a nearby unresolved source (or bright, well characterized resolved radio-object in effect serving as a *non-pointlike* calibrator), so that most of the antennas are still available for mapping. An important remaining unknown is *the maximum angular distance, between the ionospheric calibrator and the radio-field which is to be mapped, over which the "borrowed" wave parameters still describe the TEC disturbance.* This question will be addressed in coming ionospheric programs on the VLA using multi-subarray observations. To the extent that this angular

distance is *large*, then the dynamic phase-compensation scheme will be a possible approach to deconvolving transient ionospheric effects.

Regarding the wave phenomena that the VLA has already revealed, which will be treated in a separate publication, it suffices here to mention that the high-frequency, magnetic-eastward propagating disturbances have never been reported before. These waves are usually too slow to be acoustic but too short-period to be gravity waves. Their having escaped notice in previous transionospheric-refraction studies is probably due to their order-of-magnitude weaker associated phase structure (see, e.g., Figs. 10 and 11) than is the case with longer-period (gravity) waves. Moreover, many of the prior studies employ some form of selection for dominant waves, so that secondary disturbances are further suppressed in the data presentation.

Acknowledgements. The VLA is operated by the National Radio Astronomy Observatory (NRAO), which is supported by the National Science Foundation. We are indebted to several NRAO staff: for help in handling the data, G. Hunt, W. Junor, and P. Perley; for help in choosing sources and in planning the observing program, R. Perley. Moreover, we are indebted to the NRAO staff and user community for supporting this unconventional use of the VLA. This work was performed under the auspices of the U.S. Department of Energy.

Appendix A

With respect to a given source, its hour angle H is related to the local sidereal time T and to its right ascension R by

$$H = T - R. \quad (\text{A1})$$

With δ the declination and Λ the interferometer latitude, we can reexpress the local coordinates of the source as follows:

$$\sin \xi = \sin H \cos \delta \quad (\text{A2})$$

and

$$\sin \eta = \sin \delta \cos \Lambda - \cos \delta \sin \Lambda \cos H. \quad (\text{A3})$$

Letting “ Δ ” signify the difference between a parameter’s values for the s (secondary) and the p (primary) sources, we differentiate (A2 and A3) and obtain

$$\begin{aligned} \frac{\partial \Delta \sin \xi}{\partial T} &\equiv \left(\frac{\partial \sin \xi}{\partial T} \right)_{\delta_s, R_s} - \left(\frac{\partial \sin \xi}{\partial T} \right)_{\delta_p, R_p} \\ &= -(\delta_s - \delta_p) \sin \delta_p \cos H_p + (R_s - R_p) \cos \delta_p \sin H_p \quad (\text{A4}) \end{aligned}$$

and

$$\begin{aligned} \frac{\partial \Delta \sin \eta}{\partial T} &\equiv \left(\frac{\partial \sin \eta}{\partial T} \right)_{\delta_s, R_s} - \left(\frac{\partial \sin \eta}{\partial T} \right)_{\delta_p, R_p} \\ &= -(\delta_s - \delta_p) \sin \delta_p \sin \Lambda \sin H_p - (R_s - R_p) \cos \delta_p \sin \Lambda \cos H_p. \quad (\text{A5}) \end{aligned}$$

References

- Bolton J.G., Slee O.B., Stanley G.J., 1953 *AuJPh* 6, 434
- Bougeret J.L., 1981, *A&A* 96, 259
- Cirnewell T.J., Wilkonson P.N., 1981, *MNRAS* 196, 1067
- Erickson W.C., Mahoney M.J., Jacobson A.R., Knowles S.H., 1988, *Radio Sci.* 23, 273
- Hewish A.: 1951, *Proc. Roy. Soc. A* 209, 81
- Jacobson A.R., Massey R.S., Erickson W.C., 1991, *Ann. Geophys.* 9, 546
- Kelder H., Spoelstra T.A.T., 1987, *J. Atmos. Terr. Phys.* 49, 7
- Mercier C., 1986a, *Ann. Geophysicae.* 4, 469
- Mercier C., 1986b, *J. Atmos. Terr. Phys.* 48, 605
- Mercier C., Genova F., Aubier M.G., 1989, *Ann. Geophys.* 7, 195
- Meyer-Vernet N.: 1980, *A&A* 84, 142
- Meyer-Vernet N., Daigne G., Lecacheux A., 1981, *A&A* 96, 296
- Salpeter E.E., 1967, *ApJ* 147, 433
- Spoelstra T.A.T., Kelder H., 1984, *Radio Sci.* 19, 779
- Thompson A.R., Clark B.G., Wade C.M., Napier P.J., 1980 *ApJS* 44, 151
- Van Velthoven P.F.J., 1990, Medium scale irregularities in the ionospheric electron content, Thesis, Physics Department, Eindhoven University of Technology
- Van Velthoven P.F.J., Mercier C., Kelder H., 1990, *J. Atmos. Terr. Phys.* 52, 305